Effect of induced plastic strain on the porosity of PA12 printed through selective laser sintering studied by X-ray computed micro-tomography

Chiara Morano (chiara.morano@unical.it)
University of Calabria: Universita della Calabria https://orcid.org/0000-0002-8081-4092
Maria Caterina Crocco
Vincenzo Formoso
Leonardo Pagnotta

Research Article

Keywords: Additive manufacturing, Selective laser sintering, μ-CT analysis, polymer

Posted Date: September 12th, 2022

DOI: https://doi.org/10.21203/rs.3.rs-2030930/v1

Effect of induced plastic strain on the porosity of PA12 printed through selective laser sintering studied by X-ray computed micro-tomography

Chiara Morano[1,2*†], Maria Caterina Crocco[2,3†], Vincenzo Formoso[2,3,4] and Leonardo Pagnotta[1,2]

[1] Department of Mechanical, Energy and Management Engineering, University of Calabria, Via Pietro Bucci, Rende, 87036, CS, Italy.
[2] STAR Research Infrastructure, University of Calabria, Via Tito Flavio, Rende, 87036, CS, Italy.
[3] Physics Department, University of Calabria, Via Pietro Bucci, Rende, 87036, CS, Italy.
[4] Institute of Nanotechnology - Nanotec Consiglio Nazionale delle Ricerche, University of Calabria, Via Pietro Bucci, Rende, 87036, CS, Italy.

*Corresponding author(s). E-mail(s): chiara.morano@unical.it;
Contributing authors: mariacaterina.crocco@unical.it; vincenzo.formoso@unical.it; leonardo.pagnotta@unical.it;
†These authors contributed equally to this work.

Abstract

3D printing is a widespread technology in different fields, such as medicine, construction, ergonomics, and the transportation industry. Its diffusion is related to the ability of this technique to produce complex parts without needing for assembly of different components or post-processing. However, the quality of the parts produced by additive manufacturing could be affected by the fabrication process, thus leading to the development of different kinds of defects such as porosity or inclusions. Understanding the role played by these defects and promoting strategies that could help reduce their occurrence represents a key point to allow using 3D printing for structural applications. In this work, 3D printed parts have been subjected to porosity characterization by using experimental tests on Dogbones samples subjected to plastic deformation. In particular, X-ray computed micro-tomography (μ-CT) has been employed as an investigation tool for the identification of fabrication defects and for analyzing the crack growth mechanism that occurs after subjecting samples to quasi-static loading conditions.

Keywords: Additive manufacturing, Selective laser sintering, μ-CT analysis, polymer

1 Introduction

In the last decay, Additive Manufacturing (AM) has received a growing interest in different engineering fields such as automotive [1], aerospace [2] or energy [3], as well as biomedical [4], ergonomic [5], or food [6] areas. This occurrence is related to the possibility to obtain parts characterized by

complex shapes in a quite simple way thus reducing the time-to-market requirements. The method allows obtaining final parts layer by layer [7] from different raw materials, e.g., metals [8], polymers [9], or ceramics [10], as well as it could be employed for composite fabrication [11, 12], through different fabrication strategies. Among them, Power Bed Fusion (PBF) is one of the most intresting techniques since it allows obtaining parts characterized by high accuracy by employing different kinds of materials. In particular, Selective Laser Sintering (SLS) is one of the most widespread methods that permit the fabrication of a 3D object by an overlay of 2D profile layers. The powdered material is placed on a printing plate and a high-power laser is employed to selectively melt the material. Afterward, the printing plate descended of one-layer thickness, a new powder layer is deposited and the scan process is cyclically repeated until the last layer is printed. The reliability of parts obtained through the SLS technique is influenced by the process itself [13–16] and by the quality of the powder [17, 18]. In particular, 3D printed parts are subjected to geometrical error [19] and, even more crucial, to the development of inner defects, such as porosity or inclusion [20–22].

Due to that, the spread of 3D printed parts for structural applications is strictly related to the understanding of the mechanism that led to defects developing during the fabrication process, as well as the role played by them during mechanical loading [19, 23–25]. The role played by these kinds of defects on mechanical properties has been evaluated for different kinds of materials, e.g., composites [12, 26], metals [8, 27], or polymers [28, 29]. Different strategies have been employed in the last years for predicting mechanical characteristics starting from porosity measurement, e.g., analytical formulations [30, 31] or models developed from experimental measurements [10, 12, 32]. Typically, the models developed for predicting AM mechanical properties need to be corrected to take into account real pores geometry and distribution that have proven to have a high influence on mechanical properties [10, 33, 34].

For this reason, it is really important employing an adequate investigation strategy to permit defects measurement and quantification. In this way, it could be possible to improve the mechanical properties and the 3D printing process. Among different approaches proposed for porosity measurements, the μ-CT represents one of the most interesting techniques since it allows the reconstruction of the defects shapes and their distribution [35, 36]. Moreover, μ-CT allows identifying the presence of unmelted powder in 3D printed parts [21]. Overall, μ-CT is used in various fields of science, such as biology [37], material science [38, 39], geology [40], archaeology, cultural heritage [41], and engineering [42], to obtain quantitative and qualitative information.

In this paper, morphological characterization of the PA12 samples realized through SLS technology is presented. In particular, micro-computed tomography (μ-CT), has been employed for the identification of inner features of 3D printed samples. Moreover, in order to analyze the role of porosity during crack propagation, 3D printed parts have been subjected to quasi-static loading conditions to induce plastic strain. The mechanical test has been stopped at different plastic strain levels to carry out an ex-situ μ-CT analysis. This approach allows following the mechanisms that rule porosity deformation during mechanical loading, as well as their shapes and distribution.

2 Materials and method

2.1 Material

3D printed samples have been fabricated using the EOS Forminga P110 3D printer (Eos, Germany), available at the Laboratory of Physical Prototyping (LPF @STAR lab) at the University of Calabria, with a commercial nylon powder (EOSITIN P/PA2200). The 3D printer's effective building volume is equal to 200 mm x 250 mm x 330 mm, while the building speed is 20 mm^3/h. The laser type used for sintering is CO_2, 30 W.

PA2200 is a fine powder of polyamide 12 with a nominal average grain size equal to 56 μm. The material properties are reported in Tab.1 (referred to the sintered parts) [43].

Samples have been fabricated with a mixing ratio of virgin and recycled powder. The process parameters employed during sample fabrication are for the inner volume: laser power (P) 21 W, scanning speed (v) 2500 mm/s, layer thickness (δ) 0.1 mm, the hatching scan spacing (HSS) 0.25 mm, and the chamber temperature (T) 168°C. For the

Table 1: Mechanical and thermal properties of sintered parts obtained from PA2200 powder.

	Value	Unit
Melting temperature	184	^oC
Density	0.90-0.95	g/cm^3
Tensile modulus	1700±150	MPa
Tensile strength	45±3	MPa
Elongation at break	20±5	%
Flexural modulus	1240±130	MPa
Ball indentation Hardness	77.6±2	N/mm^2
Glass transition temperature	45±3	MPa

outer surface, i.e., a skin of 300 μm thickness, different values have been employed for both laser power and scanning speed, i.e., P = 16 W and v = 1500 mm/s. Therefore, the laser energy density per unit area, i.e., E_d could be calculated by using the following equation [36]:

$$E_d = \frac{P}{v * HSS} \tag{1}$$

By using the equation, the following values have been obtained for the skin and the inner volume (defined as "core") respectively: 42.6 mJ/m^2 and 33.6 mJ/m^2. Overall, by considering the percentage of total volume printed with each energy density, a value of 36.3 mJ/m^2, obtained as a weighted average of the two previous values, has been considered as the reference value for comparing results obtained in this work with data available in the literature for samples fabricated with similar energy density values.

2.2 Sample geometry and mechanical tests

The morphological characteristics of the sintered parts were studied using dogbone-shaped specimens. Samples dimensions have been chosen according to the standard ASTM-D 638-14 [44]. In particular, the type IV [44] sample geometry, has been selected for our purpose. Specimen dimensions are reported in Fig. 1 (a).

Mechanical tests have been carried out using an electromechanical testing machine, i.e., MTS model 42 (MTS Systems Corporation, USA) equipped with a 5 kN loading cell. From mechanical tests on dogbones samples, stress-strain curves were obtained. The Digital Image Correlation (DIC) technique was employed to evaluate the effective strain. The images were acquired by a GigE camera (Prosilica GT) with a maximum resolution of 2448 x 2050 pixels and a pixel size equal to 3.45 μm x 3.45 μm, a maximum frame rate of 15 fps, and a 2/3" CCD sensor (Sony ICX625). The camera, interfaced with a commercial software (Vic-Snap, Correlated Solutions), acquire images through a frame grabber (DAQ-STD-8D, National Instruments). Images have been acquired every 2 s. A workstation with a VIC-2D software package (Correlation Solution Inc., version 2009.2.0) was used to analyze the speckle images. Tensile tests have been carried out at a displacement rate equal to 0.5 mm/min. A schematic of mechanical tests carried out to follow the crack propagation mechanism is reported in Fig. 1 (b). In particular, the sample has been subjected to Δ = 10 mm elongation and, after that, the load has been removed and a μ-CT analysis has been carried out. After each unloading phase, residual plastic deformation has been detected on the sample. The procedure has been repeated until sample failure. Tests have been carried out on two different samples. For simplicity, the reported results are referred to one sample since similar results have been obtained for both dogbones.

2.3 μ-CT analysis

X-ray computed micro-tomography analysis has been carried out to identify morphological characteristics of 3D printed parts. A conventional X-ray source has been employed for μ-CT acquired data. The experimental setup, @STAR Lab at the University of Calabria, consists of a microfocus X-ray source (Hamamatsu L12161-07), a flat panel detector (Hamamatsu C7942SK-05) with a pixel size of 50 μm, and a sample positioning system. The X-Ray source emits a conical X-ray beam with a focal spot of 5 μm and an aperture angle of 43°.

The X-ray source parameters have been carefully calibrated in order to obtain high-quality images of the samples under study. The following values have been selected for the current and tube voltage respectively, i.e., 120 kV and 84 μA and, therefore, a 10 W value for the beam power, while the exposure time has been fixed to 500 ms. The sample-detector and the source-sample distance have been fixed to 200 mm. In this way, the optical magnification was equal to 2, thus obtaining

an equivalent pixel size of 25 μm. A schematic of the steps followed during μ-CT analysis for sample 3D reconstruction is reported in Fig. 2. We acquired 1800 projection images with an angular step equal to 0.2 degrees 2 (b). Subsequently, the acquired projections are normalized using flat and dark images and reconstructed 2 (c) using the Feldkamp-Davis-Kress algorithm [45]. The 3D rendering 2 (d) and the images analysis have been carried out by using software dedicated: Fiji [46] an open-source software, and Avizo a commercial one.

The tomographic reconstructions of the sample were aligned in order to identify the same area of interest for the different loading step conditions (undeformed, steps 1-5).

The pores characteristics of the dogbone-shaped specimens have been determined by gray levels segmentation.

We have eliminated from the μ-CT analysis results the smallest pores, i.e., pores with a volume lower than 2^3 voxels.

3 Results and discussion

3.1 Mechanical test

Tensile tests have been carried out to produce plastic deformation on samples and to identify the mechanical properties of additive manufactured parts. As assessed before, dogbones have been subjected to different loading-unloading steps until sample failure occurs. The Young modulus and Poisson coefficient have been obtained through Digital Image Correlation (DIC). The stress-strain curve obtained at the first loading step is reported in Fig. 3(a). In the same figure, is also reported the measured roughness value (R_a) and a typical sample profile obtained through a contact profilometer. It is possible to observe that the sample surface is characterized by a very irregular profile, with several peaks and valleys. Moreover, the R_a value, obtained as the arithmetic average of profile points vertical distance from the mean line, is significantly higher than typical values obtained for nylon realized with traditional techniques, i.e., even below 1 μm [47]. The high measured roughness could promote cracks development and reduces the sample mechanical proprieties. This aspect will be analyzed in the next paragraph. Elastic properties have been obtained through DIC analysis. Analyzing the stress-strain curve of the first step, the following parameters have been obtained: the Young modulus $E = 1.61$ GPa, the Poisson's coefficient $\nu = 0.4$, and the yield stress $S_y = 34$ MPa, in agreement with results obtained in a previous study [43, 48].

Stress-strain curves for all steps are reported in Fig. 3 (b). By considering the global behavior obtained by combining stress-strain curves for different steps, it is possible to reconstruct a typical stress-strain curve of PA12, as shown in Fig. 3 (b) by the dashed-line curve. Moreover, it is possible to observe a reduction of the plateau of the plastic strain after the first step. In the elastic region it is possible to observe the occurrence of a slope change after the second step. In fact, it is possible to observe an initial stiff region followed by a more compliant zone. Moreover, the slope change point occurs for lower stress values by increasing the step. This mechanism has been attributed to material softening due to damage accumulation and to the occurrence of high-dimension defects. Similarly, Nizina et al., [49] found a significant variation in the stress-strain curve of the sample characterized by the presence of structural defects. All results are referred to the sample 1 but similar results have been obtained for the second one.

3.2 Porosity analysis

PA12 3D printed samples, fabricated through SLS and dogbone shaped, have been employed for morphological characterization. The inner defect evolution in function of plastic strain has been evaluated by subjecting the sample to loading-unloading steps. After each loading-unloading step, the sample has been investigated by μ-CT. Porosity has been characterized qualitatively and quantitatively by considering the volume, diameter, and sphericity of the pores.

The porosity volume percentage measured at each loading-unloading step is reported in Fig. 4 (a). In particular, the total porosity volume percentage has been calculated as global pores volume divided by sample volume. Moreover, since different printing parameters have been employed for sample skin and core, porosity percentages have been calculated also in these areas. Specifically, the core porosity has been obtained as the volume of pores measured into the inner volume divided by core volume. Similarly, the skin porosity is

obtained as the volume of pores observed on the outer volume divided by skin volume. We measured a total porosity percentage of around 2.8% in the as-built condition, i.e., before the application of the external load. However, by considering only the core volume, this value increase up to 3.7% while for the skin it was found a very low porosity value, i.e., 1%, demonstrating a reduction of pores occurrence in correspondence of sample outer surface that could be attributed to the different printing parameters. In Fig. 4 (b) we show *xy*, *xz*, and *yz* sections of the undeformed sample to emphasize the pore distribution in the core volume (in gray) and in the skin volume (in orange). Overall porosity volume percentage obtained on the undeformed sample for the core is in agreement with results obtained on the same material by other authors [28, 50, 51] for samples fabricated with similar energy density values, as shown in Fig. 5. A summary of the main parameters employed in each work for samples fabrication is reported in Tab. 2.

As might be expected, porosity percentage increases by increasing the loading step, i.e., sample plastic deformation. The total porosity percentage value increases up to 4.5% at the last loading step, with an increase of 60% if compared with the undeformed sample measurement. Similarly, increments have been also observed for the core and the skin, i.e., 62% and 53% respectively. This result could be addressed to two different mechanisms: (i) an increase of the pores volume due to an external load and (ii) microcrack development that leads to pores coalescence mechanisms. Moreover, by increasing the plastic deformation, the porosity percentage increase, and the pore size become detectable: in the undeformed sample, some pores are lower than the μ-CT resolution. However, it is also possible to notice a small decrease in the porosity percentage value for both total porosity and skin porosity at the last loading step, i.e., before sample failure (Fig. 4 (a)). This result has been explained by considering the occurrence of a large crack in the last loading step at the outer surface. In fact, it is well known that, during crack propagation, the stored energy is released. For this reason, some small pores could be re-closed during crack propagation, thus they are not still detachable by μ-CT analysis. This mechanism has been further analyzed by considering porosity variation measured at three different sections, i.e., the crack section (A1), a section far from the fracture (A3), and, finally, a generic section between the previous ones (A2). Results are reported in Fig. 6. It is possible to notice an increase in the porosity in section A1 for all the analyzed loading steps that could be attributed to the crack propagation as well as to the two mechanisms described above. On the opposite, for both A2 and A3, it was observed a decrease in porosity at step 5, i.e., just before sample failure. This result confirms that the decrease is related to the energy release that occurs during crack propagation.

The occurrence of pores growth and coalescence, discussed above, is confirmed by results reported in Fig. 7. The sections shown in Fig. 7 are referred to a generic 3D cutting plane of the same sample at different loading steps, i.e., in the undeformed condition, before the load application, and at the last step, before sample failure. In Fig. 7, it is possible to notice the increase in the pore volume after sample plastic deformation. In particular, for the pore indicated by the black arrow, volume variation has been evaluated. It was found a volume increase of 92%.

Moreover, in Fig. 7 is reported the coalescence mechanisms observed after sample loading-unloading steps. This mechanism contributes to the development of inner cracks, characterized by an irregular shape, that could act as stress concentration points [27]. As before, volume increase has been evaluated and it was found a 53% increase in the overall volume.

3.3 Pores geometrical characteristics

The influence of external loading on porosity has been globally evaluated considering porosity geometrical parameters, i.e., pores volume, diameters, and sphericity. In particular, the diameter of the pores (d) and sphericity (S) were evaluated employing the following equations:

$$d = \sqrt[3]{\frac{6V}{\pi}} \tag{2}$$

$$S = \frac{\pi^{1/3}(6V)^{2/3}}{A} \tag{3}$$

where V and A are the pores' volume and pores' surface respectively. Results are reported in Fig. 8 (a), (b), and (c) while in Table 3 it

Table 2: Printig parameters employed for samples fabrication in comparison with those employed by Pavan et al. [28], by Dewful et al., [50] and by Stichel et al. [51].

	Laser power [W]	Scanning speed [mm/s]	Scan spacing [mm]	Energy Density [mJ/mm^2]	layer thickness [μm]
This work (core)	21	2500	0.25	33.6	100
This work (skin)	16	1500	0.25	42.6	100
Pavan	31.5	3000	0.3	35	120
Dewulf	44	4190	0.3	35	120
Stichel	21	2500	0.25	33.6	100

has been reported the weighted average values of each parameter for all steps, (the parameters have been weighted with respect to the number of pores observed in each class). Results are referred to the total sample, i.e., skin and core have not been evaluated separately. In fact, even if pore concentration is different for the two areas, no substantial geometrical differences have been observed between pores that occur at the skin and at the core. Parameters have been reported in function of the percentage of pores, calculated as the number of pores of each class divided by the total number of pores multiplied by 100. The analysis allows identifying the mechanism that rules samples' failure in relationship with fabrication defects.

Table 3: Weighted average values of pores volume, diameter and sphericity obtained after different loading steps.

step	volume [μm^3]	diameter [μm]	sphericity
Undeformed	1.34x10^6	126.05	0.62
Step 1	1.45x10^6	129.73	0.61
Step 2	1.72x10^6	138.23	0.60
Step 3	1.89x10^6	142.36	0.59
Step 4	2.16x10^6	146.71	0.57
Step 5	2.16x10^6	147.10	0.59

As regards the number of pores-volume plot, by moving from the undeformed condition to step 5, the number of pores characterized by a small volume decreases while the number of high volume pores increases (Fig. 8 (a)). It is important to highlight that in steps 4 and 5 has been noticed the occurrence of some pores that are characterized by a very high volume, i.e. higher than 8x10^6 μm^3. The development of these large pores is related not only to the increase of their volume due to plastic deformation but also to the coalescence phenomenon and crack propagation described previously. Moreover, as reported in Tab. 3, the volume weighted average value increases by 61 %, from 1.34x10^6 μm^3 in the undeformed condition to 2.16x10^6 μm^3 at the last step.

The diameter distribution is reported in Fig. 8 (b). The weighted average value of pores diameters in the undeformed condition was found equal to 126 μm. Overall, by increasing sample plastic deformation, it was found an increase in the pores that are characterized by higher diameters thus confirming the mechanism described above. Moreover, the average pore diameter value at the last step was found to be equal to 147 μm, with an increase of 17% if compared with the initial value. The global behavior was found to be close to results obtained on the same material by other authors [28, 50, 51] with similar values of energy density employed during 3D printing, as shown in Fig. 9. In particular, by comparing results with data obtained by Stichel et al. [51], a very similar modal value has been obtained while this value is quite lower than those obtained by the other works [28, 50]. Overall, the global distribution of the diameter curve is similar and, as obtained by Dewful et al [50] and by Stichel et al. [51], the percentage of pores that are characterized by the modal value is around 60%.

Finally, the pores' aspect ratio in function of the loading step has been analyzed through sphericity, as shown in Fig. 8 (c) and Table 3. After sample plastic deformation, the pores' aspect ratio is modified, resulting in lower sphericity values. However, moving from step 4 to step 5, it is possible to notice an inversion of the trend, i.e.,

the sphericity weighted average value increases, as reported in Tab. 3. This behavior could be attributed to energy release due to crack propagation. In fact, pores deformation has an elastic component that is released during crack propagation thus permitting pores to regain a more spherical shape. Overall, by moving from the undeformed conditions to the last loading step, pores geometry is modified, resulting in higher diameters and more irregular shapes, i.e., the sphericity weighted average value decreases by 5%, from 0.62 to 0.59.

The main interesting parameters have been correlated to further highlight the geometric modification of pores during tensile tests, as shown in Fig. 10. In particular, sphericity and surface pores' are reported in function of their volume for undeformed conditions (Figs. 10 (a) and (c)) and for the last step (Figs. 10 (b) and (d)). It is possible to notice a significant increase in pores' surface after sample plastic deformation as well as a decrease in the sphericity parameter. This behavior is accompanied by an increase in the pores' volume.

3.4 Crack propagation mechanism

The μ-CT analysis allows also to follow the crack propagation mechanism. Fig. 11 shows the crack evolution on 3D views for different loading steps. The reported 3D cutting plane of the same sample at different loading steps are referred to sections where the main crack occurs, i.e., the crack that leads to sample failure.

Cracks develop typically from the sample surface. The occurrence of porosity near to outer surface contributes to crack propagation through the coalescence mechanism. Different macroscopic cracks have been observed and, almost all of them originated from surface roughness. Moreover, the presence of inner defects, originated from large pores, modifies the sample failure mechanism. In fact, polymers typically exhibit a ductile failure mechanism, with the occurrence of a large necking area before sample fracture. Conversely, for PA12 samples it was observed a fragile failure mechanism, i.e., sudden sample collapse without any necking. Moreover, fracture surfaces are characterized by dimple morphology, with a large presence of pores. Overall, the entire section is subjected to reduction as shown by the graph reported in Fig. 12 (a). Sample profiles have been further extracted and average values at each step have been compared. It is clearly noticeable a reduction in both sample width and thickness by increasing the loading step (Fig. 12 (b)).

4 Conclusions

Additive manufactured sample morphology has been characterized through μ-CT analysis in order to evaluate the presence of production defects, i.e., porosity, as well as their influence on failure mechanism. Analysis reveals the presence of a high percentage of porosity in 3D printed parts, due to the fabrication process. Plastic deformation leads to an increase of the porosity percentage measured even if, right before sample failure, a slight decrease was observed due to the energy release mechanism. Plastic strain modify pores volume and their aspect ratio resulting in more elongated defects and, in some cases, leads to the coalescence of two or more pores into a single bigger one. That mechanism could be dangerous for structural parts since it leads to the development of macrodefects that reduce significantly sample resistance. Moreover, high roughness acts as a crack initiation point. Overall, sample failure is dominated by a fragile behavior, due to the high porosity percentage.

Acknowledgments. The Authors thank the @STAR laboratories, for providing equipment employed for experimental analysis.

Author contributions. All the authors contributed to the work design and conception. Experimental activity have been carried out by Chiara Morano and Maria Caterina Crocco and all the authors performed data measurement and analysis. Chiara Morano and Maria Caterina Crocco wrote the original draft; Vincenzo Formoso and Leonardo Pagnotta wrote, reviewed, and edited the manuscript. All authors provided critical feedback, helped with the analysis, and contributed to the final manuscript.

Funding. The work has been funded by "Progetto STAR 2 – PIR01-00008"- Ministry of University and Research.

Data availability. All authors confirm that the data supporting the findings of this study are available within the article.

Declarations

Ethics approval. The authors declare that the work has not been submitted to any other journal. The submitted manuscript is original and has not been published elsewhere in any form or language.

Consent to participate. All authors declare their voluntary agreement to participate in this research work.

Consent for publication. All authors declare their voluntary agreement to publish this research work.

Conflict of interest. The authors declare no conflict of interests.

References

[1] Leal R, Barreiros FM, Alves L, Romeiro F, Vasco JC, Santos M, et al. Additive manufacturing tooling for the automotive industry. International Journal of Advanced Manufacturing Technology. 2017 9;92:1671–1676. https://doi.org/10.1007/s00170-017-0239-8.

[2] Froes F, Boyer R. Additive manufacturing for the aerospace industry. First edition ed. Elsevier; 2019.

[3] Tarancón A, Esposito V. 3D Printing for Energy Applications. Wiley Online Library; 2021.

[4] Maniruzzaman M. 3D and 4D printing in biomedical applications: process engineering and additive manufacturing. John Wiley & Sons; 2019.

[5] Kermavnar T, Shannon A, O'Sullivan LW. The application of additive manufacturing / 3D printing in ergonomic aspects of product design: A systematic review. Applied Ergonomics. 2021 11;97. https://doi.org/10.1016/j.apergo.2021.103528.

[6] Godoi FC, Prakash S, Bhandari BR. 3d printing technologies applied for food design: Status and prospects. Journal of Food Engineering. 2016 6;179:44–54. https://doi.org/10.1016/j.jfoodeng.2016.01.025.

[7] ASTM.: Additive manufacturing-General principles-Terminology ISO/ASTM 52900:2015. ASTM International. Available from: www.iso.orgwww.astm.org.

[8] Sola A, Nouri A. Microstructural porosity in additive manufacturing: The formation and detection of pores in metal parts fabricated by powder bed fusion. Journal of Advanced Manufacturing and Processing. 2019 7;1. https://doi.org/10.1002/amp2.10021.

[9] Dizon JRC, Espera AH, Chen Q, Advincula RC. Mechanical characterization of 3D-printed polymers. Additive Manufacturing. 2018 3;20:44–67. https://doi.org/10.1016/j.addma.2017.12.002.

[10] Saâdaoui M, Khaldoun F, Adrien J, Reveron H, Chevalier J. X-ray tomography of additive-manufactured zirconia: Processing defects – Strength relations. Journal of the European Ceramic Society. 2020 7;40:3200–3207. https://doi.org/10.1016/j.jeurceramsoc.2019.04.010.

[11] Balla VK, Kate KH, Satyavolu J, Singh P, Tadimeti JGD. Additive manufacturing of natural fiber reinforced polymer composites: Processing and prospects. Composites Part B: Engineering. 2019 10;174. https://doi.org/10.1016/j.compositesb.2019.106956.

[12] Papon EA, Haque A, Mulani SB. Process optimization and stochastic modeling of void contents and mechanical properties in additively manufactured composites. Composites Part B: Engineering. 2019 11;177:107325. https://doi.org/10.1016/J.COMPOSITESB.2019.107325.

[13] Caulfield B, McHugh PE, Lohfeld S. Dependence of mechanical properties of polyamide components on build parameters in the SLS process. Journal of Materials Processing Technology. 2007 2;182:477–488. https://doi.org/10.1016/j.jmatprotec.2006.09.007.

[14] du Plessis A. Effects of process parameters on porosity in laser powder bed fusion revealed

by X-ray tomography. Additive Manufacturing. 2019 12;30. https://doi.org/10.1016/j.addma.2019.100871.

[15] Moussaoui K, Rubio W, Mousseigne M, Sultan T, Rezai F. Effects of Selective Laser Melting additive manufacturing parameters of Inconel 718 on porosity, microstructure and mechanical properties. Materials Science and Engineering A. 2018 9;735:182–190. https://doi.org/10.1016/j.msea.2018.08.037.

[16] Pavan M, Faes M, Strobbe D, Van Hooreweder B, Craeghs T, Moens D, et al. On the influence of inter-layer time and energy density on selected critical-to-quality properties of PA12 parts produced via laser sintering. Polymer Testing. 2017 03;61:386–395.

[17] Vock S, Klöden B, Kirchner A, Weißgärber T, Kieback B. Powders for powder bed fusion: a review. Progress in Additive Manufacturing. 2019;4(4):383–397.

[18] Zhang Z, Yao XX, Ge P. Phase-field-model-based analysis of the effects of powder particle on porosities and densities in selective laser sintering additive manufacturing. International Journal of Mechanical Sciences. 2020 1;166. https://doi.org/10.1016/j.ijmecsci.2019.105230.

[19] Malekipour E, El-Mounayri H. Common defects and contributing parameters in powder bed fusion AM process and their classification for online monitoring and control: a review. The International Journal of Advanced Manufacturing Technology. 2018 03;95. https://doi.org/10.1007/s00170-017-1172-6.

[20] Al-Maharma AY, Patil SP, Markert B. Effects of porosity on the mechanical properties of additively manufactured components: a critical review. Materials Research Express. 2020 12;7. https://doi.org/10.1088/2053-1591/abcc5d.

[21] Kim FH, Moylan SP, Garboczi EJ, Slotwinski JA. Investigation of pore structure in cobalt chrome additively manufactured parts using X-ray computed tomography and three-dimensional image analysis. Additive Manufacturing. 2017 10;17:23–38. https://doi.org/10.1016/j.addma.2017.06.011.

[22] Maskery I, Aboulkhair NT, Corfield MR, Tuck C, Clare AT, Leach RK, et al. Quantification and characterisation of porosity in selectively laser melted Al–Si10–Mg using X-ray computed tomography. Materials Characterization. 2016;111:193–204. https://doi.org/https://doi.org/10.1016/j.matchar.2015.12.001.

[23] Ghanekar AS, Crawford RH, Watson D. Optimization of SLS process parameters using D-optimality. In: 2003 International Solid Freeform Fabrication Symposium; 2003. .

[24] Zarringhalam H, Hopkinson N, Kamperman N, De Vlieger J. Effects of processing on microstructure and properties of SLS Nylon 12. Materials Science and Engineering: A. 2006;435:172–180.

[25] Wegner A, Witt G. Correlation of process parameters and part properties in laser sintering using response surface modeling. Physics Procedia. 2012;39:480–490.

[26] Wang X, Jiang M, Zhou Z, Gou J, Hui D. 3D printing of polymer matrix composites: A review and prospective. Composites Part B: Engineering. 2017;110:442–458.

[27] Liu W, Chen C, Shuai S, Zhao R, Liu L, Wang X, et al. Study of pore defect and mechanical properties in selective laser melted Ti6Al4V alloy based on X-ray computed tomography. Materials Science and Engineering A. 2020 10;797. https://doi.org/10.1016/j.msea.2020.139981.

[28] Pavan M, Craeghs T, Van Puyvelde P, Kruth JP, Dewulf W. Understanding The Link Between Process Parameters, Microstructure And Mechanical Properties Of Laser Sintered Pa12 Parts Through X-ray Computed Tomography. Procedia of the 2nd International Conference on Progress in Additive Manufacturing. 2016 05;.

[29] Wang X, Zhao L, Fuh JYH, Lee HP. Effect of Porosity on Mechanical Properties of 3D Printed Polymers: Experiments and Micromechanical Modeling Based on X-ray Computed Tomography Analysis. Polymers. 2019;11(7). https://doi.org/10.3390/polym11071154.

[30] Choren JA, Heinrich SM, Silver-Thorn MB. Young's modulus and volume porosity relationships for additive manufacturing applications. Journal of Materials Science. 2013 8;48:5103–5112. https://doi.org/10.1007/s10853-013-7237-5.

[31] Leuders S, Vollmer M, Brenne F, Tröster T, Niendorf T. Fatigue strength prediction for titanium alloy TiAl6V4 manufactured by selective laser melting. Metallurgical and materials transactions A. 2015;46(9):3816–3823.

[32] Siddique S, Imran M, Rauer M, Kaloudis M, Wycisk E, Emmelmann C, et al. Computed tomography for characterization of fatigue performance of selective laser melted parts. Materials and Design. 2015 06;83:661–669. https://doi.org/10.1016/j.matdes.2015.06.063.

[33] Kasperovich G, Haubrich J, Gussone J, Requena G. Correlation between porosity and processing parameters in TiAl6V4 produced by selective laser melting. Materials and Design. 2016 9;105:160–170. https://doi.org/10.1016/J.MATDES.2016.05.070.

[34] Carlton HD, Haboub A, Gallegos GF, Parkinson DY, MacDowell AA. Damage evolution and failure mechanisms in additively manufactured stainless steel. Materials Science and Engineering: A. 2016;651:406–414.

[35] du Plessis A, Sperling P, Beerlink A, Tshabalala L, Hoosain S, Mathe N, et al. Standard method for microCT-based additive manufacturing quality control 1: Porosity analysis. MethodsX. 2018 1;5:1102–1110. https://doi.org/10.1016/j.mex.2018.09.005.

[36] Flodberg G, Pettersson H, Yang L. Pore analysis and mechanical performance of selective laser sintered objects. Additive Manufacturing. 2018;24:307–315. https://doi.org/https://doi.org/10.1016/j.addma.2018.10.001.

[37] Brombal L, Donato S, Dreossi D, Arfelli F, Bonazza D, Contillo A, et al. Phase-contrast breast CT: the effect of propagation distance. Physics in Medicine and Biology. 2018;63(24):24NT03.

[38] Stelitano S, Rullo A, Piredda L, Mecozzi E, Di Vito L, Agostino RG, et al. The Deltah Lab, a New Multidisciplinary European Facility to Support the H2 Distribution and Storage Economy. Applied Sciences. 2021;11(7). https://doi.org/10.3390/app11073272.

[39] Ferraro M, Mangini F, Sun Y, Zitelli M, Niang A, Crocco M, et al. Multiphoton ionization of standard optical fibers. Photonics Research. 2022;10:1394–1400. https://doi.org/10.1364/PRJ.451417.

[40] Donato P, Donato S, Barba L, Crisci G, Crocco M, Davoli M, et al. Influence of Chemical Composition and Microvesiculation on the Chromatic Features of the Obsidian of Sierra de las Navajas (Hidalgo, Mexico). Minerals. 2022 01;12:177. https://doi.org/10.3390/min12020177.

[41] López Prat M, Agostino R, Ray Bandyopadhyay S, Carrascosa B, Crocco M, Luca R, et al. Architectural Terracruda Sculptures of the Silk Roads: New Conservation Insights Through a Diagnostic Approach Based on Non-Destructive X-ray Micro-Computed Tomography. Studies in Conservation. 2021 01;p. 1–13. https://doi.org/10.1080/00393630.2020.1862605.

[42] Conte R, Filosa R, Formoso V, Gagliardi F, Agostino RG, Ambrogio G. Analysis of extruded pins manufactured by friction stir forming for multi-material joining purposes. In: AIP Conference Proceedings. vol. 2113. AIP Publishing LLC; 2019. p. 050026.

[43] EOS.: PA2200 - Material data sheet. EOS GmbH.

[44] ASTM.: D 638-00 Standard Test Method for Tensile Properties of Plastics 1. Available from: www.astm.org.

[45] Feldkamp LA, Davis LC, Kress JW. Practical cone-beam algorithm. Journal of the Optical Society of America A. 1984;1(6):612–619.

[46] Schindelin J, Arganda-Carreras I, Frise E, Kaynig V, Longair M, Pietzsch T, et al. Fiji: an open-source platform for biological-image analysis. Nature methods. 2012;9(7):676–682.

[47] Thompson R, Austin D, Wang C, Neville A, Lin L. Low-frequency plasma activation of nylon 6. Applied Surface Science. 2021;544:148929.

[48] Alfano M, Morano C, Bruno L, Muzzupappa M, Pagnotta L. Analysis of debonding in bio-inspired interfaces obtained by additive manufacturing. Procedia Structural Integrity. 2018;8:604–609. AIAS2017 - 46th Conference on Stress Analysis and Mechanical Engineering Design, 6-9 September 2017, Pisa, Italy. https://doi.org/https://doi.org/10.1016/j.prostr.2017.12.059.

[49] Nizina T, Nizin D, Kanaeva N, Artamonov D. Method for analyzing the kinetics of damage accumulation in the structure of polymer materials under tensile stresses. AIP Conference Proceedings. 2021;2371(1):020010. https://doi.org/10.1063/5.0059899.

[50] Dewulf W, Pavan M, Craeghs T, Kruth JP. Using X-ray computed tomography to improve the porosity level of polyamide-12 laser sintered parts. Cirp Annals. 2016;65(1):205–208.

[51] Stichel T, Frick T, Laumer T, Tenner F, Hausotte T, Merklein M, et al. A Round Robin study for selective laser sintering of polymers: Back tracing of the pore morphology to the process parameters. Journal of Materials Processing Technology. 2018;252:537–545.

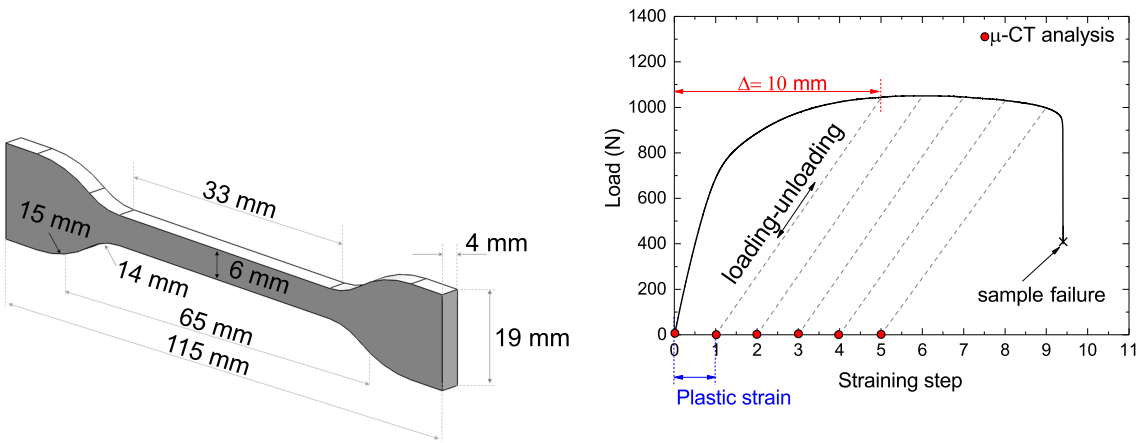

(a) (b)

Fig. 1: (a) Schematic of Dogbones samples employed for mechanical characterization and (b) loading steps representation.

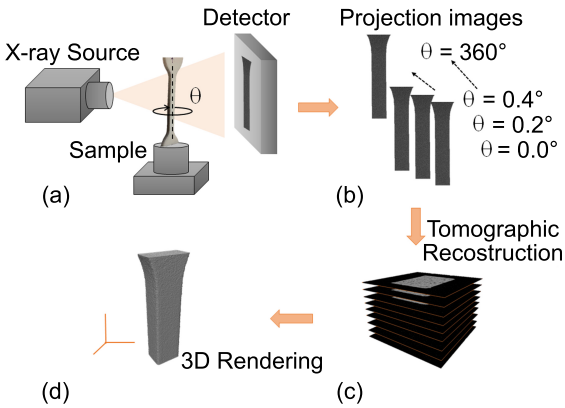

Fig. 2: (a) Illustration of the μ-CT set-up. (b) Set of projections at different rotation angles. (c) Slices of the sample. (d) 3D rendering of the sample.

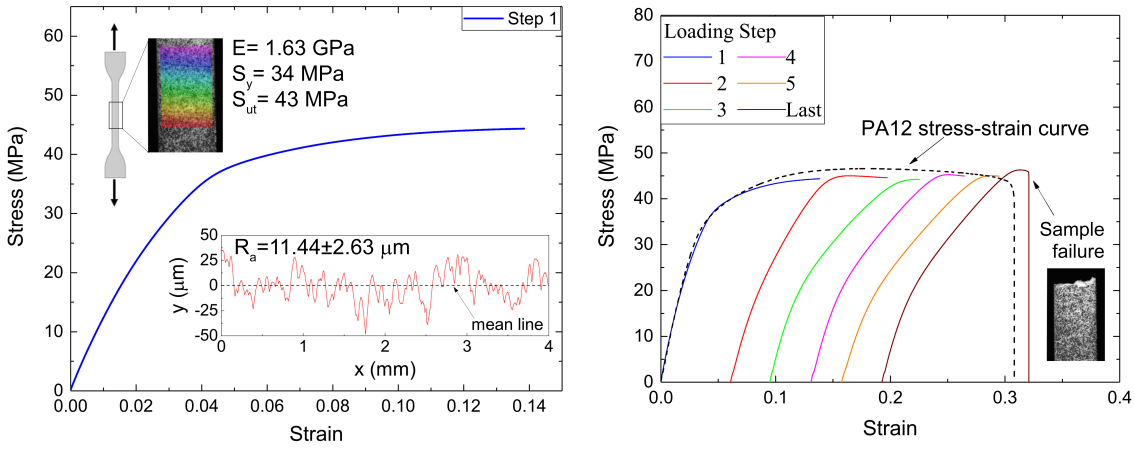

(a) (b)

Fig. 3: (a)Stress-strain behavior obtained at the first loading step and (b) stress-stain curves for different steps.

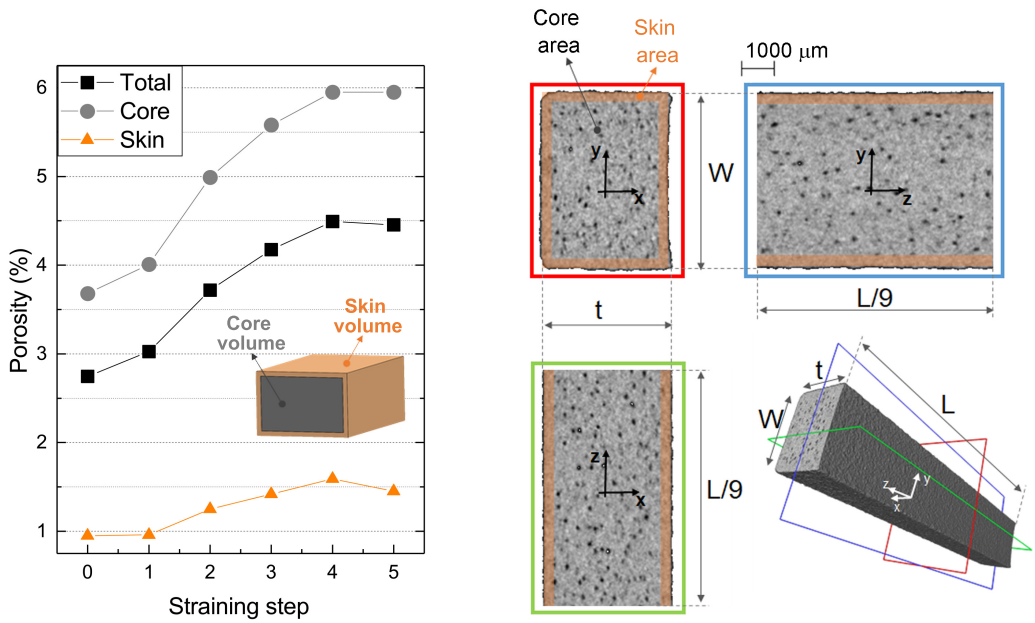

(a) (b)

Fig. 4: (a) Porosity percentage in function of loading step for total sample, the core and the skin (zero point is referred to undeformed condition) (b) porosity distribution along sample (the green, red and blue rectangles represent the sections location).

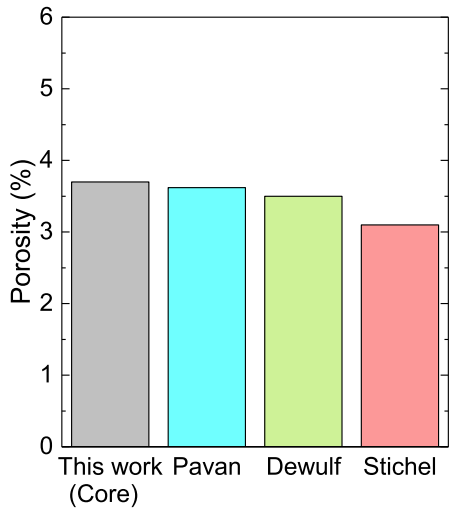

Fig. 5: Porosity percentage in comparison with results obtained by Pavan et al. [28], by Dewful et al., [50] and by Stichel et al. [51].

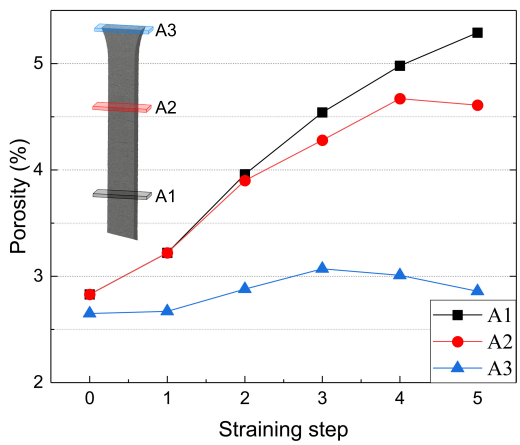

Fig. 6: Porosity evolution in function of loading step for different sample section (zero point is referred to undeformed condition).

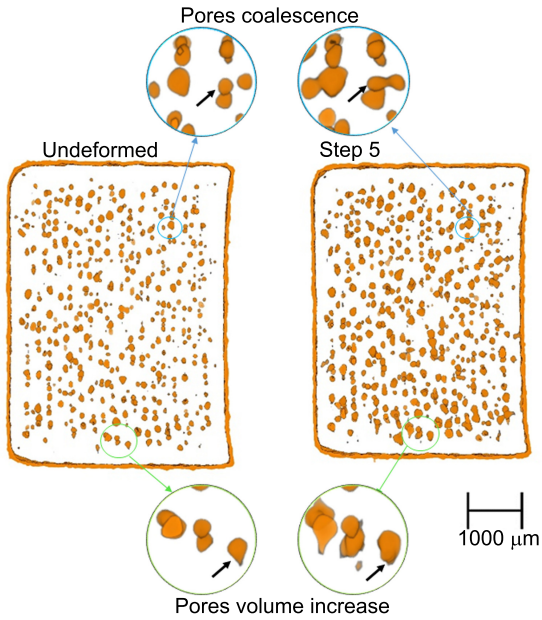

Fig. 7: Mechanisms involved during samples plastic deformation: pores volume increases and pores coalescence.

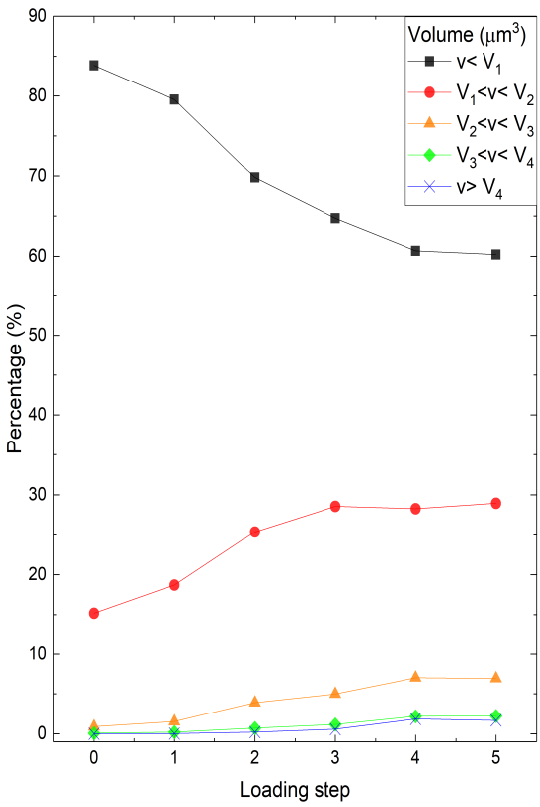

(a)

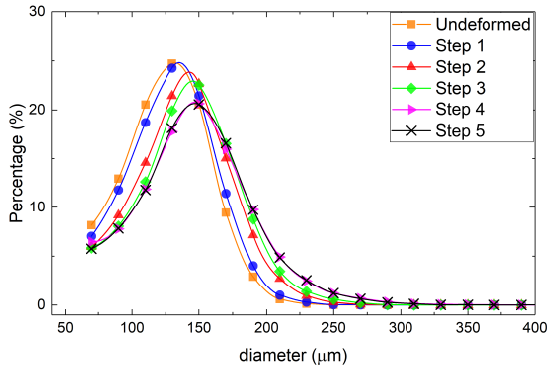

(b)

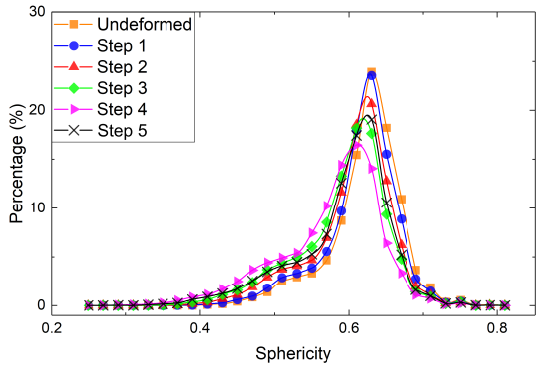

(c)

Fig. 8: (a) Percentage of pores with different volume values in function of loading steps, where $V_1 = 2$ x 10^6 μm^3, $V_2 = 4$ x 10^6 μm^3, $V_3 = 6$ x 10^6 μm^3, $V_4 = 8$ x 10^6 μm^3; (b) Percentage of pores with different diameters and (c) sphericity in function of loading step (where 1 is obtained for a perfect sphere).

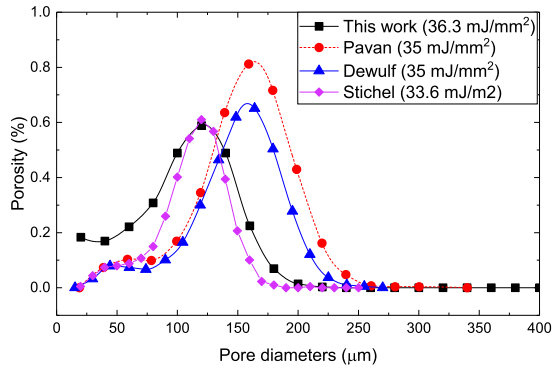

Fig. 9: Equivalent diameter behavior in comparison with results obtained by Pavan et al. [28], by Dewful et al., [50] and by Stichel et al. [51].

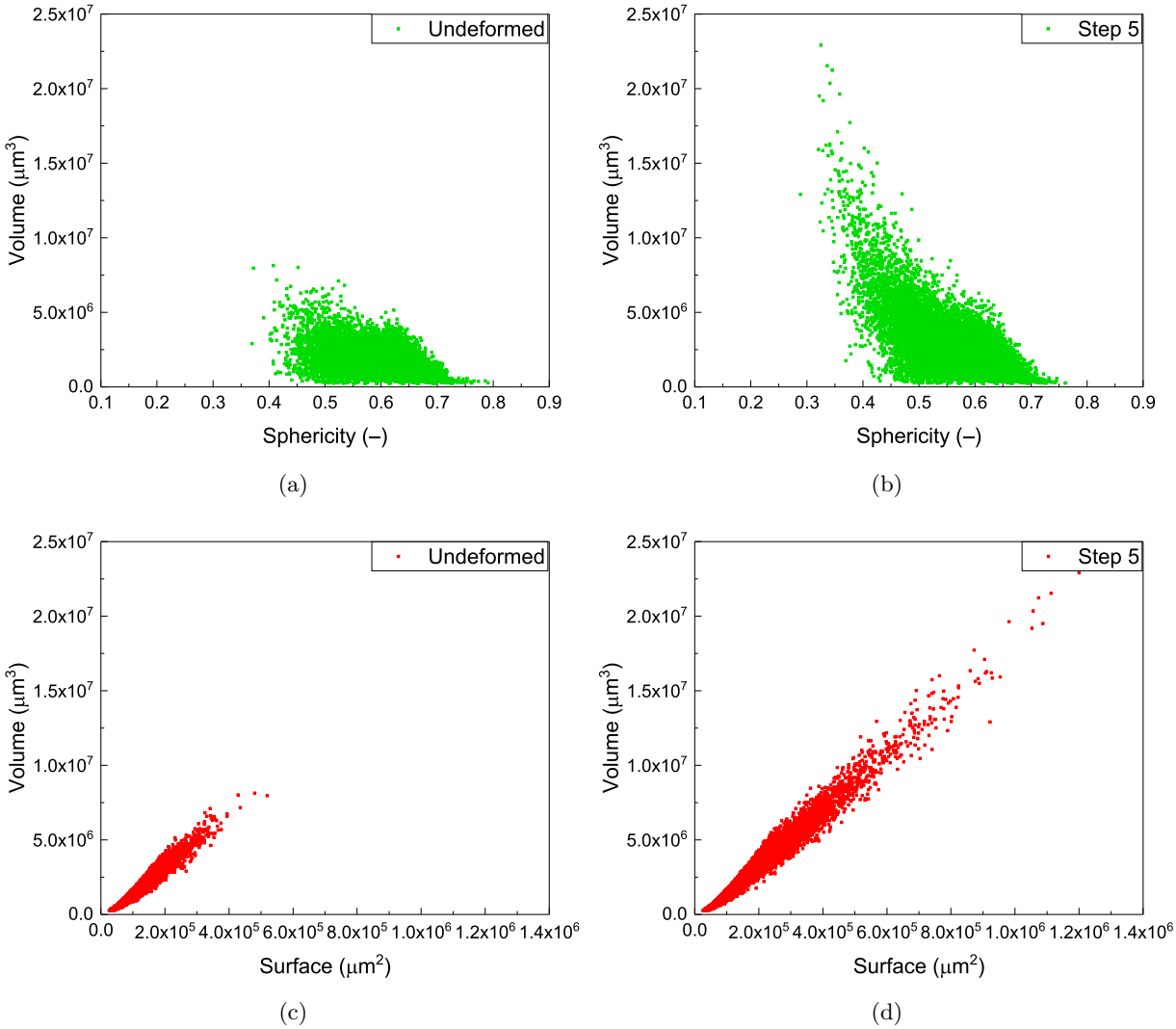

Fig. 10: (a) Pores volume in function of sphericity (where 1 is obtained for a perfect sphere) and (b) Pores volume in function of pores surface.

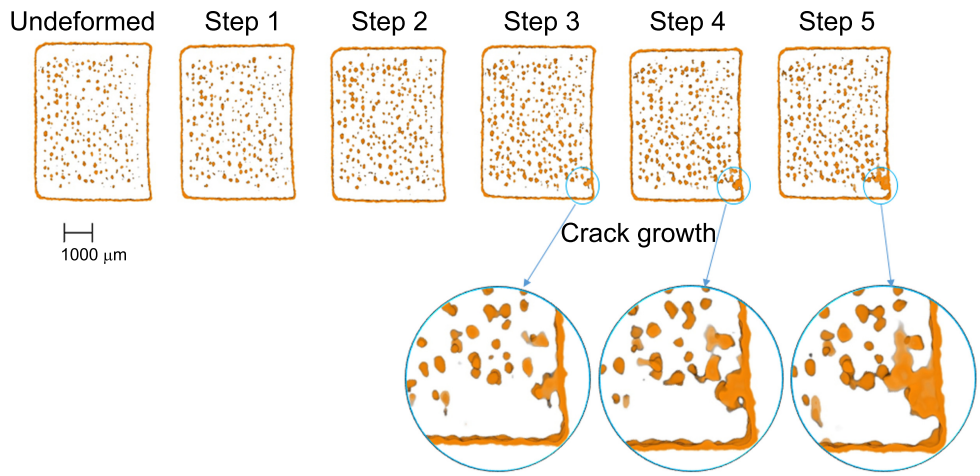

Fig. 11: Crack propagation mechanism. The reported images are referred to sections where the main crack occurs.

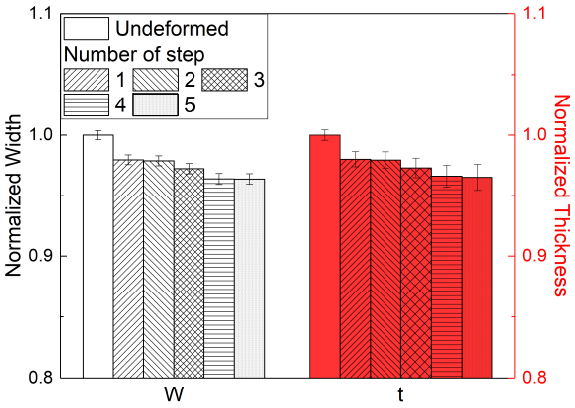

(a)

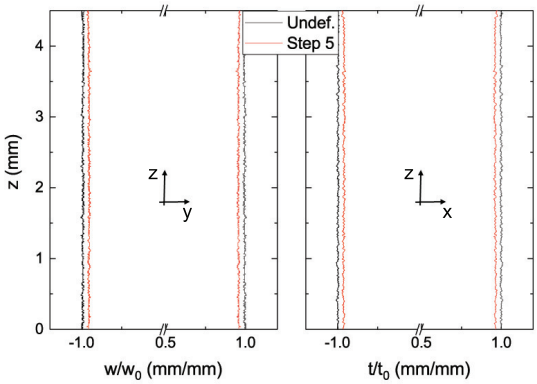

(b)

Fig. 12: (a) Normalized sample thickness and width at different loading steps (b) Normalized sample profiles in undeformed condition and at step 5 (dimensions are not in scale).